Quantum System Dynamics and the Quasistatic Approximation

Andrew Hudson and James Camparo*

*Photonics Technology Department, Physical Sciences Laboratories, The Aerospace Corporation, PO Box 92957,
Los Angeles, California 90009, USA*

Understanding the dynamics of quantum systems to time-varying perturbations is not only a question of basic physics, it is a question that can have life-critical relevance. Specifically, as GPS signals take on greater roles in autonomous navigation, means must be found to ensure the moment-by-moment integrity of those signals, and thereby the integrity of GPS atomic clock frequencies. The frequency of an electromagnetic field, like the microwave field in a GPS atomic clock, is stabilized to a quantum system's energy structure by modulating the field's frequency and then demodulating the quantum system's response. The first harmonic (i.e., fundamental) demodulated signal provides the correction for field frequency, while the second harmonic is often taken as an instantaneous status-of-health indicator for the correction signal. The *interpretative* problem for the second harmonic is that the modulation frequency, the quantum system's dephasing rate, and the Rabi frequency are all approximately equal in these frequency stabilization systems, violating the textbook assumptions of quantum mechanics: the quasistatic approximation (QSA), the adiabatic approximation, and the sudden approximation. Here, we take a careful experimental and theoretical look at the QSA under realistic conditions for field stabilization (i.e., the approximation most often employed for the engineering interpretation of atomic dynamics behavior). Our results demonstrate that the second harmonic can be employed as a rapid-response herald of correction signal degradation, and that while the QSA is useful as a means for diagnosing causal effects through the second harmonic, a small-signal approximation (SSA) is better.

I. INTRODUCTION

Often, when the frequency of an electromagnetic (EM) field is locked to a quantum system for sensing purposes, the field's wavelength is modulated at ω_m and allowed to resonantly interact with the quantum system as illustrated in Fig. 1 [1]. Routinely, the atoms' dynamics are detected and demodulated at the fundamental of the modulation frequency, yielding the atoms' "first-harmonic response" S_1, which creates the frequency-correction signal for the field. When the applied EM field is on resonance $S_1 = 0$, otherwise the sign and magnitude of S_1 provide information on the sign and magnitude of the field's detuning: $\Delta \equiv \nu_f - \nu_o$. (Here, ν_f is the EM field's frequency, while ν_o is the quantum system's resonant frequency.) As a sensor, the stabilized EM field can be employed to measure Doppler shifts, magnetic field strengths, or integrated to measure time intervals (i.e., atomic clocks).

The figure of merit for this kind of sensor, and thereby the inherent capability of the atomic device, is defined by the slope of the fundamental signal on resonance (i.e., $dS_1/d\Delta|_{\Delta=0}$). This slope is a measure of the correction signal's ability to discriminate against small deviations between the field's frequency and the atom's resonant frequency, and intuitive discussions of the device's functioning and figure of merit usually proceed via the quasistatic approximation (QSA). In the QSA, the dynamics are viewed in terms of the quantum system's *static* response to the resonant field. Thus, in the QSA S_1 is proportional to the static lineshape's first derivative, while the second-harmonic signal S_2 (demodulated at $2\omega_m$) is proportional to the second derivative of the static lineshape. To the extent that the QSA is valid, S_2 is a measure of $dS_1/d\Delta|_{\Delta=0}$ [2], and can therefore be employed as an atomic signal figure-of-merit or status-of-health indicator [3,4].

For researchers in the laboratory, the QSA has the advantage of yielding relatively simple closed-form expressions for $dS_1/d\Delta|_{\Delta=0}$ that *qualitatively* capture the atomic system's dependence on various parameters (e.g., dephasing rate γ_2 and Rabi frequency Ω). Consequently, the QSA can be a useful guide for researchers desiring rapid information on design trade-offs, and suggestions for profitable directions of device improvement (see, for example, Ref. [5]). Nevertheless, in most situations of real practical interest the QSA is *quantitatively* questionable, since it assumes that the atomic system reaches steady state in the time interval between "significant" field variations. Specifically, given adiabatic fast passage effects
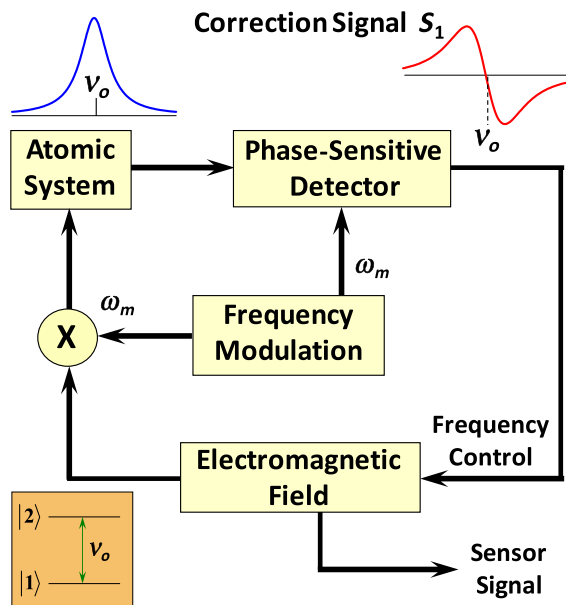
_____
*james.c.camparo@aero.org

FIG. 1. Basic frequency feedback loop of an atomic device. The frequency of an electromagnetic field undergoes wavelength modulation at some relatively low rate ω_m, and interacts with a quantum system causing the atoms to undergo a state change, $|1\rangle \leftrightarrow |2\rangle$. The atoms' response to the wavelength-modulated electromagnetic field is monitored using phase-sensitive detection (i.e., the atoms' response is demodulated at ω_m), which produces a correction signal that keeps the frequency, ν_f, of the EM field locked to the atoms' resonant frequency, ν_o. The stabilized electromagnetic field can then be used in diverse ways for sensing (e.g., magnetic fields, time intervals, and Doppler shifts).

[6,7] maximum values of $dS_1/d\Delta|_{\Delta=0}$ are obtained when $\omega_m \sim \gamma_2$, strongly invalidating the QSA. Further, since $dS_1/d\Delta|_{\Delta=0}$ is maximized near saturation, atomic devices routinely operate with $\Omega \sim \gamma_2$ (and as a consequence $\Omega \sim \omega_m$). Therefore, none of the standard approximations found in quantum mechanics textbooks apply to real atomic devices [8,9]: the QSA is violated, since $\omega_m \sim \gamma_2$; the sudden approximation is violated, since ω_m is not much faster than all other rates; and the adiabatic approximation is violated, since Ω is not much greater than ω_m.

The failure of these approximations' underpinnings would pose no real problem if all atomic devices were confined to the laboratory, where one can always appeal to numerical solutions of the time-dependent Schrödinger equation. This, however, is not the case, since atomic devices have now moved well beyond the research laboratory's confines. As a dramatic illustration, the satellites of GPS and other global navigation satellite systems (GNSS) carry atomic clocks as they orbit the Earth at an altitude of 12 000 miles. In such cases, the onboard atomic devices need to autonomously and rapidly estimate their status of health, and provide to ground operators (through space-to-ground telemetry links) information on the

atomic system's functioning. One of the clearest examples of this need concerns passenger aircraft navigating their runway approaches using GPS [10]. In that situation, GPS signal-integrity algorithms do not have the luxury of running highly accurate, multilevel, Runge-Kutta atomic dynamics codes. GPS spacecraft must autonomously evaluate the status of health of their onboard clocks second by second in order to protect lives, and rapidly provide operators on the ground with information so that they can quickly make informed decisions regarding the present and future health of the satellite clock.

This then raises the basic physics question of the present work: *given that the validity conditions of the QSA are strongly violated, yet the QSA is effectively the "go to" tool for easily interpreting the relationship between* $dS_1/d\Delta|_{\Delta=0}$ *and* S_2 *(with* S_2 *provided by space-to-ground telemetry), how badly corrupted are the QSA's predictions of quantum-system dynamics*? Saying this differently (and more in line with a specific application), given that the validity conditions of the QSA are violated in GNSS atomic clocks, can systems engineers and operators nonetheless employ the simple closed-form expressions of the QSA to interpret atomic clock health warnings? The predictions of the QSA do not need to be accurate at the fractions of a percent level. Rather, systems engineers and operators need to know if a significant (e.g., 20%) drop in S_2 implies a significant problem with the onboard atomic clock; and therefore that users should ignore that satellite's signal in their navigation solutions until such time as ground-station device engineers can examine the situation more judiciously. Somewhat surprisingly, the answer to that question is presently unknown.

To be clear, assessing GPS *signal integrity* can be achieved in a number of ways: for example, with receiver autonomous integrity monitoring (RAIM), where multiple (redundant) computations of position can be exploited to determine the internal consistency of the navigation solutions [10], or by the self-monitoring of oscillator signals using delayed frequency comparisons [11]. These techniques can alert users and ground controllers that there is a problem with a GNSS satellite's signal, but they cannot isolate that problem to the atomic physics package of the satellite atomic clock, nor can they suggest what may have been the root cause of the problem. Examination of the second-harmonic signal has that potential, if theoretical approximations can be trusted for S_2 interpretations.

Here, we take a look at the relationship between $dS_1/d\Delta|_{\Delta=0}$ and S_2 in an atomic clock system, and there are three basic and applied general atomic physics questions that we look to answer:

1. How (if at all) is S_2 *quantitatively* related to $dS_1/d\Delta|_{\Delta=0}$ under conditions that are known to violate the QSA?

2. Even if quantitatively inaccurate, to what extent is the QSA's prediction of *proportionality* between S_2 and $dS_1/d\Delta|_{\Delta=0}$ valid?

3. Even if quantitatively inaccurate, and even if S_2 is not exactly proportional to $dS_1/d\Delta|_{\Delta=0}$, is the QSA "good enough" for systems engineering applications? Is the QSA good enough to be used as an autonomous *diagnostic* of atomic clock health in life-critical GNSS applications?

In the next section, we discuss the QSA in more detail, as well as another less-well-known approximation that can lead to closed-form expressions relating S_2 to $dS_1/d\Delta|_{\Delta=0}$: the small-signal approximation (SSA). Then, in Sec. III we discuss our experiment examining S_2 and $dS_1/d\Delta|_{\Delta=0}$ as functions of Ω. In Sec. IV the experimental results are compared to the QSA, the SSA, and a numerical density-matrix computation. Finally, based on our measurements we discuss the utility of S_2 as a status-of-health *interpreter* for remote vapor-cell atomic clocks, like those flying on GNSS satellites.

II. QUASISTATIC AND SMALL-SIGNAL APPROXIMATIONS

A. Quasi-static approximation

With the QSA, one assumes that the modulation period of the field, $2\pi/\omega_m$, is long compared to the time scale of atomic processes, so that the atoms effectively reach steady state at each instantaneous value of the modulated field's frequency. Consequently, writing $\Delta(t)$ as $\Delta_o + \alpha\omega_m g(t)$ [where α is the modulation index, Δ_o is the average field and atom detuning, and $g(t)$ is a modulation waveform, for example $g(t) = \sin(\omega_m t)$], the atoms' response to the modulated field, $\Sigma(t)$, can be expanded in a Taylor series about Δ_o, yielding

$$\Sigma(t) = \Sigma(\Delta_o) + \alpha\omega_m g(t) \frac{d\Sigma}{d\Delta}\bigg|_{\Delta_o}$$
$$+ \frac{1}{2}[\alpha\omega_m g(t)]^2 \frac{d^2\Sigma}{d\Delta^2}\bigg|_{\Delta_o} + \dots \quad (1)$$

For sine wave modulation, it is straightforward to show that at the average detuning Δ_o

$$\Sigma(t) = S_o + S_1 \sin(\omega_m t) + S_2 \cos(2\omega_m t) + \dots, \quad (2)$$

where

$$S_o \cong \Sigma(\Delta_o) + \frac{\alpha^2\omega_m^2}{4} \frac{d^2\Sigma}{d\Delta^2}\bigg|_{\Delta_o}, \quad (3a)$$

$$S_1 \cong \alpha\omega_m \frac{d\Sigma}{d\Delta}\bigg|_{\Delta_o}, \quad (3b)$$

$$S_2 \cong -\frac{\alpha^2\omega_m^2}{4} \frac{d^2\Sigma}{d\Delta^2}\bigg|_{\Delta_o} \cong -\frac{\alpha\omega_m}{4} \frac{dS_1}{d\Delta}\bigg|_{\Delta_o}. \quad (3c)$$

Thus, in the QSA we have on resonance

$$\left|\frac{dS_1}{d\Delta}\right| = \frac{4|S_2|}{\alpha\omega_m}. \quad (4)$$

(In what follows when writing $|dS_1/d\Delta|$ it is assumed that this is evaluated at $\Delta_o = 0$.)

Taking the routine case that $\Sigma(\Delta_o)$ corresponds to a saturated Lorentzian, we have

$$\Sigma(\Delta_o) = \left(\frac{\Omega^2}{\Omega_s^2 + \Omega^2}\right)\left(\frac{\gamma_2^2 + \frac{\gamma_2}{\gamma_1}\Omega^2}{\gamma_2^2 + \Delta_0^2 + \frac{\gamma_2}{\gamma_1}\Omega^2}\right), \quad (5)$$

where γ_1 is the longitudinal relaxation rate and Ω_s is the saturation Rabi frequency. The first term in brackets in this expression accounts for saturation of the signal amplitude, while the second accounts for power broadening of the Lorentzian lineshape. Using Eq. (5) in Eq. (3c), we find that

$$S_2 = \frac{\alpha\omega_m}{2(\gamma_2^2 + \frac{\gamma_2}{\gamma_1}\Omega^2)}\left(\frac{\Omega^2}{\Omega_s^2 + \Omega^2}\right). \quad (6)$$

It is important to note that in the demodulation process, the experimental results for $dS_1/d\Delta$ and S_2 will have units of (for example) V/Hz and V, respectively. However, in what follows we want to compare theory and experiment, and so we need a common unit of measurement for the signal, $\Sigma(t)$, that applies to both experiment and theory. We therefore define normalized values of $|dS_1/d\Delta|$ and $|S_2|$:

$$X_1' \equiv \frac{\left|dS_1/d\Delta\right|}{\left|dS_1/d\Delta\right|_M}, \quad (7a)$$

$$X_2 \equiv \frac{4|S_2|/\alpha\omega_m}{\left|dS_1/d\Delta\right|_M}, \quad (7b)$$

where $|dS_1/d\Delta|_M$ is the *maximum* value of $|dS_1/d\Delta|$. (In the present experiments, this is the maximum value of $|dS_1/d\Delta|$ as a function of Rabi frequency for fixed γ_2 and ω_m.)

In contrast to the normalized values, and contemplating the utility of S_2 as a herald and interpreter of changes in $dS_1/d\Delta$ (complimentary to other heralds of change), what is important are the fractional changes of $|S_2|$ from its *nominal* value, and how those relate to fractional changes in $|dS_1/d\Delta|$ from its nominal value. Therefore, to examine the

utility of S_2 as a status-of-health indicator and interpreter, we define two additional parameters:

$$Y_1' = \left(\frac{\left| dS_1/d\Delta \right|}{\left| dS_1/d\Delta \right|_M} - 1 \right) = X_1' - 1, \qquad (8a)$$

$$Y_2 = \frac{|S_2|}{|S_2|_N} - 1. \qquad (8b)$$

In Eqs. (8), we assume that the nominal value of $|dS_1/d\Delta|$ is equal to $|dS_1/d\Delta|_M$ (i.e., the system is designed for optimal frequency-stabilization purposes, so that nominally $|dS_1/d\Delta|$ takes on its maximum value), and we define $|S_2|_N$ as the value of $|S_2|$ *when $|dS_1/d\Delta|$ achieves its maximum value*. With this definition of Y_2, we are explicitly noting that $|S_2|_N$ may not equal the maximum value of $|S_2|$ as a function of Rabi frequency. To be clear, Y_1' and Y_2 represent fractional changes in $|dS_1/d\Delta|$ and $|S_2|$ from their values under optimum frequency-stabilization conditions, while X_1' and X_2 represent normalized values of $|dS_1/d\Delta|$ and $|S_2|$ relative to a common normalization constant.

B. Small-signal approximation

In the atomic candle [12–14], the second harmonic is employed to stabilize the *amplitude* of an electromagnetic field, and in their studies of the Rabi resonances employed in atomic candles Coffer *et al.* [15] considered the dynamics of an atom's response to a phase-modulated resonant field [i.e., $g(t) = \sin(\omega_m t)$]. Specifically, Coffer *et al.* considered solutions to the system's density-matrix equations based on a "small-signal" approximation [16].

Writing the density matrix as $\boldsymbol{\rho}(t) = \langle \boldsymbol{\rho}(t) \rangle + \boldsymbol{\delta}(t)$, where $\langle \boldsymbol{\rho}(t) \rangle$ represents an unmodulated portion of the density matrix's evolution (which can eventually reach steady state) and $\boldsymbol{\delta}(t)$ an addition to the density matrix that accounts for the atoms' modulated dynamics, the SSA requires in a quasi-steady-state limit that $\text{Im}[\langle \rho_{12} \rangle] > \text{Im}[\delta_{12}]$. (Here, ρ_{12} is the density-matrix coherence term for a two-level atom.) With the additional assumption that $\alpha \omega_m \gg \gamma_2$, Coffer *et al.* then obtained closed-form expressions for the atoms' first- and second-harmonic responses to the phase-modulated field, yielding on resonance:

$$\left. \frac{dS_1}{d\Delta} \right|_{\Delta_o = 0} \cong -\frac{\Omega^2 \alpha \omega_m}{2[\gamma_2^2 + (\gamma_2/\gamma_1)\Omega^2]\sqrt{(\Omega^2 - \omega_m^2)^2 + \gamma_1^2 \omega_m^2}}, \qquad (9a)$$

$$S_2 \cong \frac{\Omega^2 \alpha^2 \omega_m \gamma_2}{4[\gamma_2^2 + (\gamma_2/\gamma_1)\Omega^2]\sqrt{(\Omega^2 - 4\omega_m^2)^2 + 4\gamma_1^2 \omega_m^2}}. \qquad (9b)$$

Thus, in the SSA we have on-resonance

$$\left| \frac{dS_1}{d\Delta} \right| = \frac{4|S_2|}{\alpha \omega_m} F\left(\frac{\Omega}{\gamma_2}, \frac{\omega_m}{\gamma_2}, \frac{\gamma_1}{\gamma_2} \right), \qquad (10a)$$

where

$$F\left(\frac{\Omega}{\gamma_2}, \frac{\omega_m}{\gamma_2}, \frac{\gamma_1}{\gamma_2} \right) = \frac{\omega_m}{2\gamma_2} \sqrt{\frac{(\Omega^2 - 4\omega_m^2)^2 + 4\gamma_1^2 \omega_m^2}{(\Omega^2 - \omega_m^2)^2 + \gamma_1^2 \omega_m^2}}. \qquad (10b)$$

In situations where $\Omega \sim \omega_m \sim \gamma_2$ and $\gamma_1 \cong \gamma_2$ (i.e., the situation applicable to GNSS atomic clocks, but clearly a violation of the SSA's underlying assumptions) Eq. (10a) simplifies to

$$\left| \frac{dS_1}{d\Delta} \right| \cong \frac{4\sqrt{3}|S_2|}{\alpha \omega_m}. \qquad (11)$$

III. EXPERIMENT AND RESULTS

Figure 2 is a block diagram of our experimental arrangement, where we employ the 6834.7 MHz 0-0 hyperfine transition in ^{87}Rb [i.e., $5^2 S_{1/2}(F_g = 2, m_F = 0) - 5^2 S_{1/2}(F_g = 1, m_F = 0)$] to study the relationship between $dS_1/d\Delta$ and S_2. A vertical cavity surface emitting laser (VCSEL) at $\lambda = 780$ nm is locked to the $5^2 S_{1/2}(F_g = 2) \rightarrow 5^2 P_{3/2}$ transition of ^{87}Rb (i.e., the D_2 transition) in a cell containing isotopically enriched Rb and 10 torr of N_2. In a separate beam, the same laser light is expanded and apertured (to make a reasonably collimated "top-hat" beam) before passing into our resonance cell, which also contains isotopically enriched ^{87}Rb and 10 torr N_2. (Given the relatively large phase noise of VCSEL diode lasers [17], and the not so small diameter of our aperture, we see no evidence of diffraction effects in our experiment or our experimental results.) The beam diameter in the resonance cell is $2R_L \cong 0.27$ cm; the cell has a diameter of $2R_c = 2.5$ cm, and the cell length is $L = 3.8$ cm. This geometry is chosen so that the signal volume diameter will be much smaller than the cell diameter, thereby limiting temperature gradients across the signal volume to the axial direction. The maximum laser power entering the cell is nominally 45 μW, and the laser light optically pumps the ^{87}Rb atoms creating a population imbalance between the two ground-state hyperfine manifolds. As a consequence of optical pumping, there is a reduction in the number density of atoms in the optically absorbing $|F_g = 2, m_F\rangle$ Zeeman states [18,19].

The cell is located in an oven where we impose a compensating temperature gradient along the cell length to mitigate naturally occurring, systematic, axial temperature gradients. The oven sits inside a mu-metal tube to limit environmental magnetic fields to the axial direction, and the "heating jacket" is actually composed of two strip
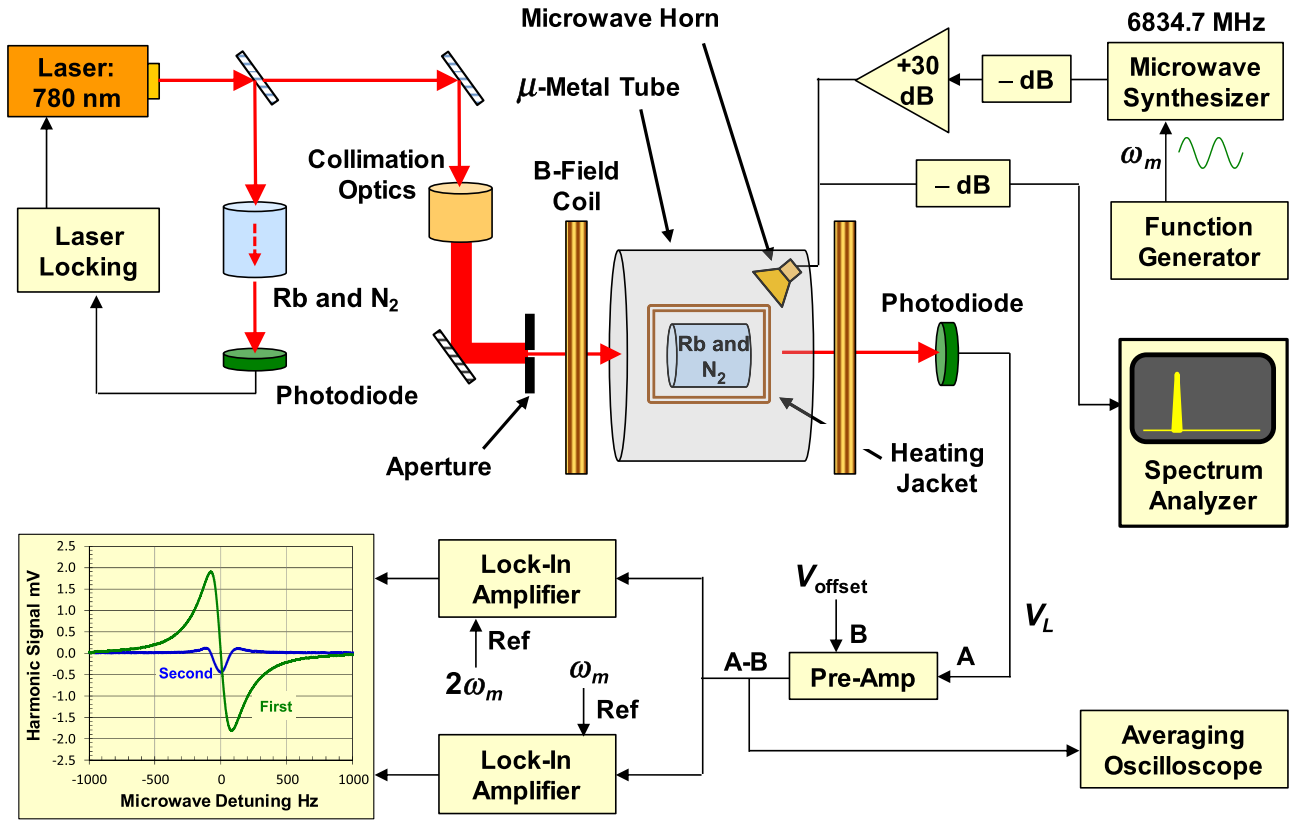
FIG. 2.   Experimental arrangement. With heating strips placed on the front and back of the resonance cell (i.e., "heating jacket") we can compensate potential temperature gradients along the length of the cell. Since the beam diameter is small, we should be insensitive to transverse temperature gradients.

heaters on each end of the cell. Nominally, the temperature of the resonance cell is 44 °C, corresponding to a measured optical attenuation coefficient of $\xi[\mathrm{Rb}]\sigma L = 2$ [[Rb] is the Rb number density; the fraction of absorbing atoms in the optically excited hyperfine manifold is $\xi = (I+1)/(2I+1) = 5/8$ with I the nuclear spin of ^{87}Rb, and σ is the optical absorption cross section]. Magnetic field coils are placed outside the mu-metal tube in order to impose a controllable, axial quantization axis on the atoms, and these provide a 76-mG magnetic field inside the tube. The microwaves at 6834.7 MHz are derived from a frequency synthesizer; they pass through a variable attenuator, and then a +30-dB amplifier before passing to a horn that broadcasts the microwave signal to the atoms in the resonance cell. Since the microwave field is free space, there is no cavity-mode field geometry over the signal volume that could create mesoscopic effects [20].

The transmitted light intensity is detected with a Si photodiode and amplified. As the microwave field is tuned about the 0-0 hyperfine resonance, the number density of atoms in the absorbing state increases, tracing out the microwave resonance in the absorbed laser light. For maximum optical pumping and consequently maximum signals we use full laser intensity, and from

previous studies this yields a γ_2 of 85 Hz [21]. From those same studies we also know the microwave power at this light intensity that yields a near-optimum 0-0 resonance lineshape for microwave frequency-stabilization purposes (i.e., a lineshape near saturation): $P = -11$ dBm as measured on the spectrum analyzer. We label this optimum microwave power P_N (i.e., nominal operating condition).

From those same studies we were able to determine the correlation between spectrum-analyzer measured power and power-broadened linewidth (i.e., half-width at half-maximum, $\Delta\nu_{1/2}$): $\Delta\nu_{1/2} = \beta\sqrt{P}$ with $\beta = (316 \pm 28)$ Hz/mW$^{1/2}$ extrapolated to zero light intensity [22]. The value of β at zero light intensity is relevant, since it allows a calibration of Rabi frequency to β without assumptions regarding the value of a light-dependent linewidth enhancement factor [23]. Specifically, in the limit of zero light intensity $\beta\sqrt{P} = \sqrt{\gamma_2/\gamma_1}\,\Omega$. In the present situation, where the Carver rate is small [24] and diffusional relaxation likely dominates [25,26] we expect $\gamma_2/\gamma_1 \cong 1$. Consequently, at the nominal power P_N we estimate $\Omega_N = (89 \pm 8)$ Hz. Measuring the amplitude of the fundamental signal as a function of Rabi frequency, we are

TABLE I. Listing of the dynamical parameters that optimize the slope of the first-harmonic signal for frequency-stabilization purposes in the present experiment.

Dynamical parameter	Value
Measured dephasing rate at full light γ_2	85 Hz
Nominal Rabi frequency Ω_N	(89 ± 8) Hz
Saturation Rabi frequency Ω_S	(74 ± 7) Hz
Modulation frequency ω_m	81.73 Hz
Modulation depth $\alpha\omega_m$	33 Hz

also able to determine the saturation Rabi frequency: $\Omega_s = (74 \pm 7)$ Hz.

For the present experiments, we are interested in the modulated response of the atoms to the resonant microwave field as a function of Δ_o. Consequently, we set $\Delta = \Delta_o + \alpha\omega_m\sin(\omega_m t)$, and demodulated the signal from the photodetector with two lock-in amplifiers, one was referenced to ω_m and the other to $2\omega_m$. With each lock in we obtain both the in-phase and quadrature components of the demodulated signal, which allows us to reconstruct the magnitudes of S_1 and S_2: $|S_j| = [S^2_{j,\text{inphase}} + S^2_{j,\text{quad}}]^{1/2}$. The four lock-in outputs are recorded and averaged for a number of Δ_o scans in order to improve the measured signal-to-noise ratio, and $|dS_1/d\Delta|$ is computed from the magnitude of S_1 as a function of Δ_o.

With $\Omega = \Omega_N$, we investigate ranges of modulation frequency and modulation index that would maximize the slope of the fundamental signal on resonance. We find that maximum values of $|dS_1/d\Delta|$ are obtained with $\omega_m = 81.73$ Hz and $\alpha = 0.404$. (Additionally, we want a value of ω_m that would be very incompatible with ac
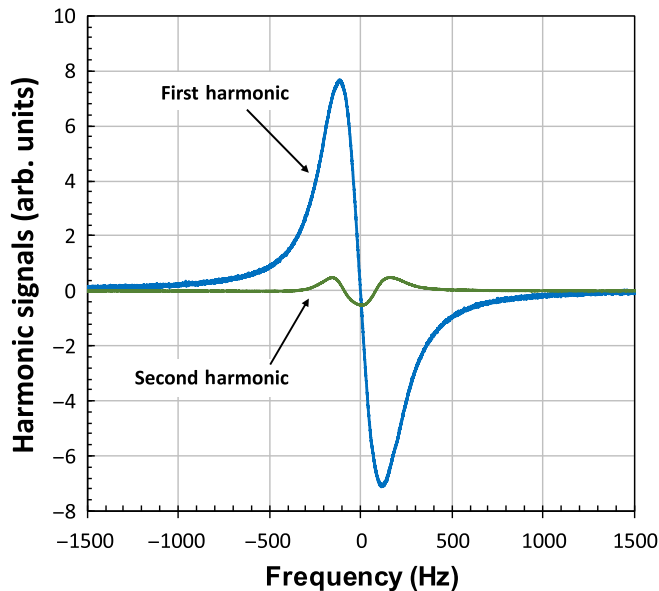
line voltage.) The complete set of dynamical parameters for our experimental situation are provided in Table I, and as discussed previously the dynamical parameter values that maximize $|dS_1/d\Delta|$ lead to violations of the standard approximations employed in atomic physics: $\omega_m \sim \Omega_N \sim \gamma_2$. Figure 3 shows an example of the in-phase S_1 and S_2 signals as functions of Δ_o for the case of $P/P_N = 1.56$; and as one would expect from the QSA the fundamental has the appearance of a Lorentzian lineshape's first derivative, while the second harmonic has the appearance of a second derivative. For each trial, we determine the resonant frequency by finding the zero crossing of $|S_1|$.

Determining the magnitude of S_2 on resonance is straightforward: it is just the vector sum of the lock-in amplifier's in-phase and quadrature second-harmonic signals when $\Delta_o = 0$. However, determining the magnitude of $|dS_1/d\Delta|$ requires some discussion. Specifically, the tangent line to the first derivative of a Lorentzian varies near $\Delta_o = 0$ (albeit slightly). Consequently, it is not always best to simply fit a straight line to the first-harmonic data in some region about $\Delta_o = 0$ to determine $|dS_1/d\Delta|$, as this could introduce systematic errors into the results. Since our digitized fundamental signals are separated by a frequency interval of $\delta f = 0.34$ Hz, we settle on the following procedure: (1) using the $|S_1|$ data, we compute the numerical derivative of our fundamental signal: $\delta|S_1|/\delta f$; (2) these $\delta|S_1|/\delta f$ values are fit by a quadratic function in a ± 50 Hz region about $\Delta_o = 0$ (i.e., $\delta|S_1|/\delta\Delta = a\Delta^2 + b$); (3) the intercept is taken as our estimate of $|dS_1/d\Delta|$. Figure 4 shows an example of this procedure.

FIG. 3. Example of our first- and second-harmonic signals (in-phase components) as functions of Δ_o for $P/P_N = 1.56$.

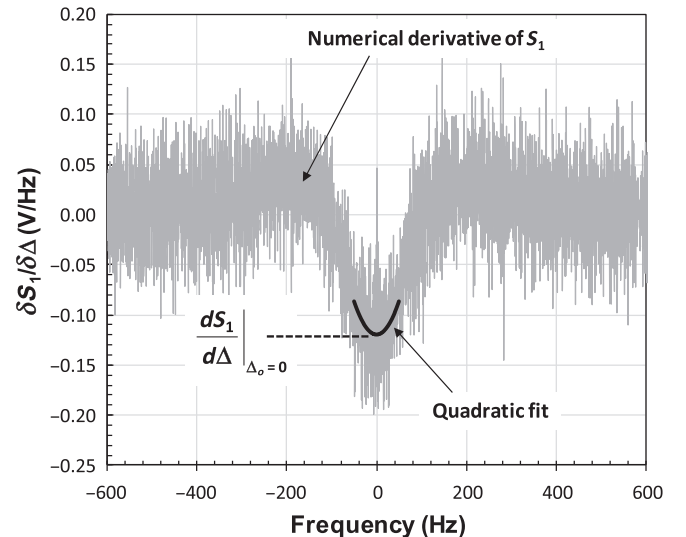
FIG. 4. Example of our determination of $|dS_1/d\Delta|$ for $P/P_N = 1.56$. The numerical derivative has been smoothed over a 1-Hz bandwidth for clarity of presentation. However, for the actual analyses the quadratic fits are taken over unsmoothed data: $\delta|S_1|/\delta\Delta = a\Delta^2 + b$, with the intercept of the fit providing our estimate of $|dS_1/d\Delta|_{\Delta o=0}$.
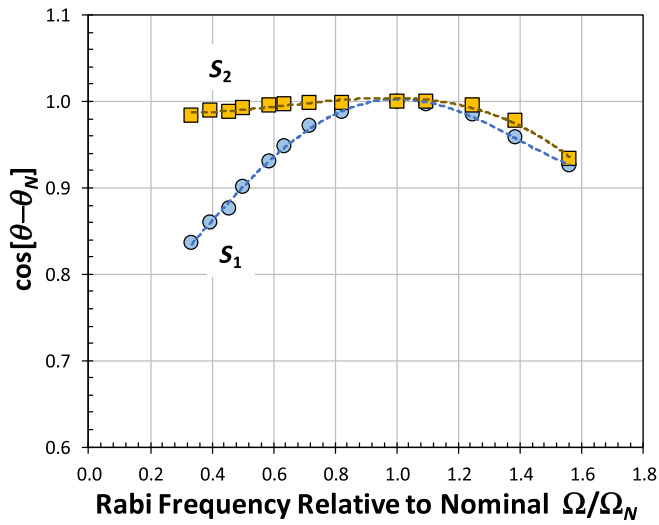
FIG. 5.   In our experiments, we chose the lock-in phase θ by maximizing the in-phase signal of each lock-in amplifier at $\Omega = \Omega_N$: for the first harmonic we find $\theta_N = -52.3°$, while for the second harmonic $\theta_N = -40.2°$. As Ω changes, without readjusting θ, the in-phase signal will scale like $\cos[\theta - \theta_N]$ all other things being equal. As the figure shows, for both the first-harmonic and second-harmonic signals, $\cos[\theta - \theta_N]$ varies slowly near $\Omega = \Omega_N$. The dashed lines are simply aids to guide the eye.

Figure 5 shows the cosine of the phase difference for S_1 (or S_2) from its nominal value as a function of Rabi frequency (i.e., $\theta =$ the signal phase at Ω, and $\theta_N =$ the signal phase at Ω_N). For both S_1 and S_2 the cosine of the phase difference changes slowly near $\Omega \cong \Omega_N$. This implies that an examination of S_1 and S_2 magnitudes (i.e., the vector sum of the in-phase and quadrature signals) should provide valid information on the in-phase behavior of these signals alone for Ω near Ω_N.

IV. EXPERIMENT AND THEORY COMPARISON

The experimental measurements of the normalized first-harmonic slope, X'_1, are shown in Fig. 6(a), and agree very well with the density-matrix calculations (discussed in Appendix A). In particular, it should be noted that there are no free parameters in the density-matrix calculations. The experimental results are in fair agreement with the QSA at low Ω, but much better agreement with the SSA. At high Ω, experiment and the density matrix remain in agreement. However, while the density matrix remains in fair agreement with the QSA in the regime of high Ω, it is in poor agreement with the SSA. To understand this behavior, note that there is a transition in the approximate theories' agreement with the density matrix: in weak fields the SSA is better than the QSA, while in strong fields the reverse tends to be true. We rationalize this by recognizing that the SSA assumptions are best satisfied in weak fields, and will break down under saturation conditions. Alternatively, in strong fields the dressed states of the atom become well separated in energy, so that modulation cannot induce nonadiabatic transitions between the dressed states [6]. For all intents and purposes in strong fields the atom's response is something close to quasistatic, because we can consider the modulation as a perturbation *acting on the dressed-atom eigenfunctions of the static dressed-atom Hamiltonian.*
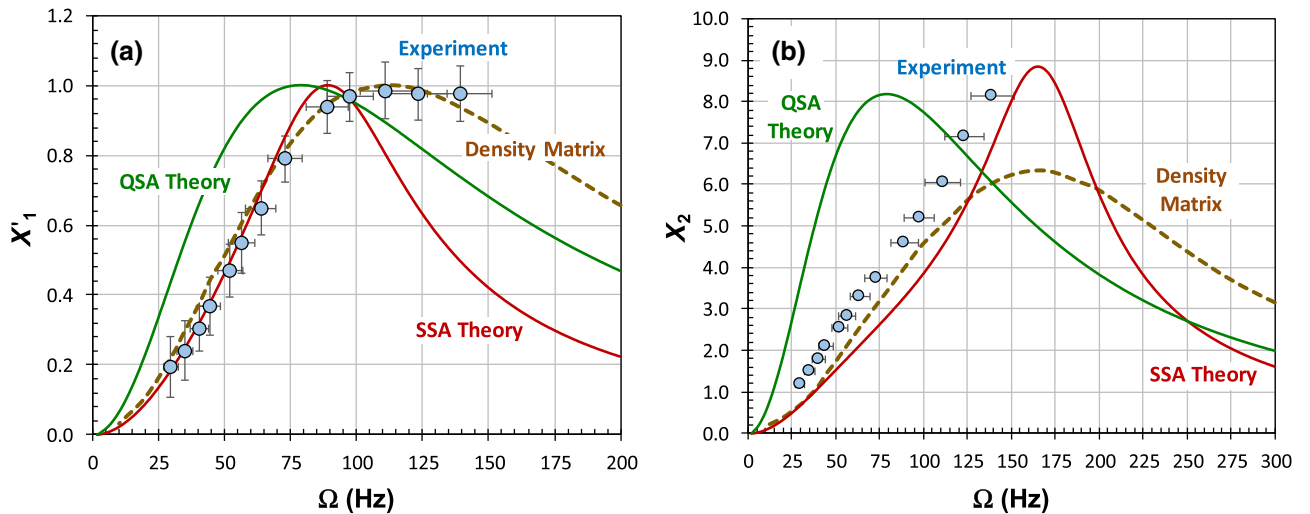

FIG. 6.   (a) Normalized slope of the first-harmonic signal X'_1 and (b) the normalized magnitude of the second-harmonic signal X_2 as functions of the Rabi frequency Ω. Circles correspond to the experimental results, and the dashed line is a density-matrix calculation discussed in Appendix A. Also shown are predictions from the QSA theory and the SSA theory. In (b), the divergence of the experimentlal results and the density matrix in strong fields (i.e., $\Omega > \Omega_N$) is thought to be due to higher-order diffusion modes as discussed more fully in Appendix B, which are not adequately modeled in the present density-matrix equations.

The second-harmonic signal as a function of the Rabi frequency is shown in Fig. 6(b), and again we note reasonable agreement between experiment and the density matrix in weak fields. The slight disagreement between density-matrix theory and experiment in weak fields that we do notice is easily explained as a consequence of not adequately estimating the rate parameters (e.g., the Rabi frequency). Additionally, similar to Fig. 6(a) the SSA agrees better with the density matrix than the QSA in weak fields. However, as Ω approaches saturation experiment and the density matrix diverge. Though at present we have no complete explanation for this strong-field divergence, we do have a working hypothesis. In the present work we approximate diffusion's effect on the density matrix's evolution through the γ_1 and γ_2 relaxation parameters. Though this is a routine approximation for dealing with diffusion [27], it is nonetheless a coarse one [18,28]. As discussed in Appendix B, the various diffusion modes that enter the problem have differing influences on the atom's first- and second-harmonic responses, and the higher-order diffusion modes play a more significant role in the atomic system's second-harmonic dynamics than the first-harmonic dynamics as microwave power saturates the atomic transition. In the present work, with a beam diameter much smaller than the resonance-cell diameter, we clearly excite higher-order radial diffusion modes [26,28].

Figure 7 shows the relationship between $|dS_1/d\Delta|$ and S_2 relative to their nominal values: Y'_1 as a function of Y_2. Interestingly, experiment agrees reasonably well with the QSA theory, the SSA theory and the density matrix in weak fields: all three theories imply near proportionality between $|dS_1/d\Delta|$ and S_2, and this is what is observed experimentally. Though it would appear that experiment agrees better with the QSA and SSA theories in weak fields than the density matrix, we take this more as coincidence than any real indication of QSA and SSA theory superiority. As noted with regard to the strong-field divergence between experiment and the density matrix in Fig. 6(b), it is likely that the present density-matrix equations do not fully account for the details of diffusional relaxation, and it may be that with regard to the relationship between $|dS_1/d\Delta|$ and S_2 the QSA and SSA are more forgiving of these deficiencies.

In strong fields (i.e., $Y_2 > 0$) not only do experiment and the density matrix diverge in Fig. 7 [likely for the same working-hypothesis reason as discussed with regard to Fig. 6(b)], but the SSA theory fails badly in its agreement with the density matrix. Alternatively, the QSA theory is in fair agreement with the density matrix for both weak and strong fields. From Eq. (3c), it is easy to show that the QSA theory is restricted to Y'_1 and Y_2 less than zero. Therefore, as the Rabi frequency transitions weak $\rightarrow$ strong, the QSA theory marches Y_2 to the right with Y'_1 increasing; as the Rabi frequency transitions strong $\rightarrow$ weak, Y_2 marches to the left with Y'_1 now decreasing as it retraces its weak $\rightarrow$ strong path.
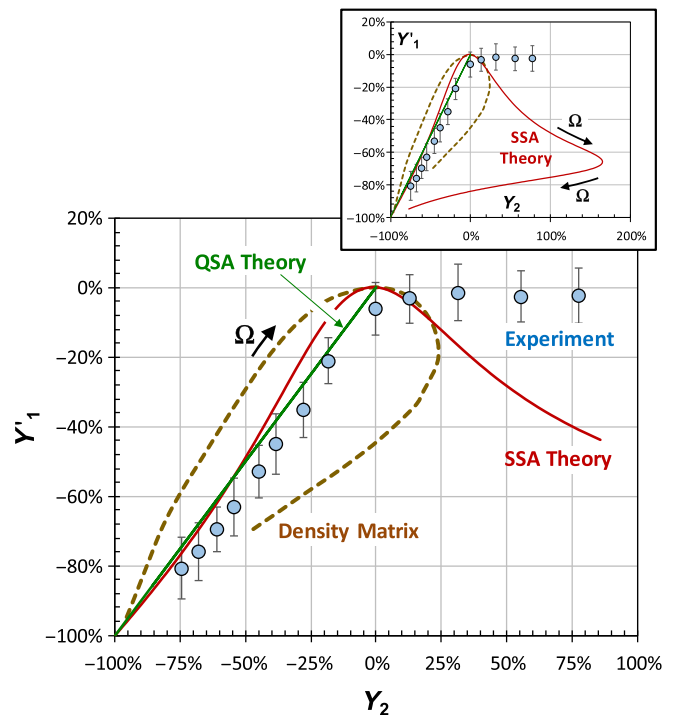

FIG. 7. Change in $|dS_1/d\Delta|$ relative to its nominal value, Y'_1, as a function of the change in $|S_2|$ relative to its nominal value Y_2. In weak fields (i.e., $\Omega < \Omega_N \Rightarrow Y_2 < 0$) experiment and all three theories are in reasonable agreement. We note that the QSA is restricted to Y'_1 and Y_2 less than zero. In strong fields the SSA is in complete disagreement with the density-matrix calculations and experiment, while the QSA simply retraces its path from $Y_2 = 0$ to $Y_2 = -1.0$. For completeness, the inset shows the SSA theory over the full range of Ω.

V. DISCUSSION

Given the results of Figs. 6 and 7, we are in a position to address the questions raised in Sec. I. First, with regard to proportionality and the quantitative relationship between $|dS_1/d\Delta|$ and $|S_2|$... it depends. In weak fields, changes in $|S_2|$ reasonably reflect proportional changes in $|dS_1/d\Delta|$. In strong fields, the density-matrix calculations suggest that the proportional relationship is weakened, while the experiment and theory comparison indicates that unmodeled physical processes (i.e., higher-order diffusional relaxation modes) completely negate the proportional relationship. As far as employing theory to diagnose causal effects given an observed *decrease* in $|S_2|$ from its nominal value (and by inference a decrease in $|dS_1/d\Delta|$ from its nominal value), the Fig. 6 data suggest that while the QSA theory is not bad, the SSA theory is better.

As noted in Sec. I, there are a number of ways GNSS users can be alerted to problems in a satellite's navigational message (e.g., RAIM). However, simply alerting users to a potential problem is only part of the issue. Users, and

more importantly ground controllers, should have information on the source of the problem (e.g., the onboard atomic clock) and the possible mechanism creating that problem. This latter is important for ground controllers, since it provides pathways of response (e.g., deciding on whether the onboard clock should be turned off and another on, or allowing the problem time to self-correct); it is also valuable for users, since it can provide information on how long the satellite's navigational message may be unavailable. In this context, the second-harmonic signal is an adjunct to other means of integrity monitoring: (1) it can confirm a problem with the GNSS satellite's navigational message; (2) it can pinpoint the source of the problem to the onboard atomic clock; and (3) when combined with other telemetry information [29,30] can limit possible atomic clock degradation mechanisms.

Of course, taken together Figs. 6 and 7 indicate that $|S_2|$ can *only* be employed as a herald and interpreter of changes in $|dS_1/d\Delta|$ for decreases in $|S_2|$ from its nominal value. If $|S_2|$ increases, "all bets are off." However, with regard to integrity monitoring and problem interpretation for life-critical GNSS signals, we are not concerned with *increases* (i.e., betterment) of $|dS_1/d\Delta|$. There is no integrity-monitoring user-alert scenario one can reasonably envision where the onboard clock performs *better* than expected. To protect the integrity of GPS signals we are primarily concerned with sudden and unexpected degradation and failures of atomic clock components. For example, a change in microwave power from its optimum value [31], due perhaps to radiation effects on a clock's step-recovery diode [32], or some decrease in the quality factor of the atomic clock's microwave cavity [33]. Thus,

1. for integrity-monitoring and problem-interpretation purposes, decreases in $dS_1/d\Delta|_{\Delta=0}$ are proportional to (and heralded by) decreases in S_2;
2. for integrity-monitoring and problem-interpretation purposes, our results indicate that both the QSA and SSA can be employed to diagnose atomic clock health issues, with the SSA likely the better choice.

VI. CONCLUSION

Twenty years ago atomic sensors based on frequency-stabilized electromagnetic fields were not necessarily rare, but they were certainly not ubiquitous. Today that situation has changed with the proliferation of (for example) atomic magnetometers and atomic clocks [34]. Importantly, the reliability of atomic devices in crucial infrastructure, the miniaturization of atomic devices, and the enhancement of atomic device performance, are all problems that straddle basic and applied science. One the one hand, the resolution of those problems will not be found through complex numerical solutions of the Schrödinger equation that provide little intuitive guidance, nor will they be found through empirical engineering charts on the other. Rather, their solution will require a mix of basic and applied science: physically based, intuitive, and valid approximations of atomic dynamics under time-dependent perturbation conditions that can help guide the efforts of electrical, mechanical, and systems engineers.

In this work, we show that the QSA and the SSA have value for those endeavors. Both theories of quantum-system dynamics are reasonably good approximations to more rigorous density-matrix descriptions of the dynamics, with the SSA likely a better approximation in weak fields and the QSA a better approximation in strong fields. Of course the present work also illustrates that there appears to be more detail in the dynamics than even a reasonably complete density-matrix calculation provides, and our present thinking is that this derives from the complex role of diffusional relaxation in the dynamics. We plan to investigate this further in future work.

APPENDIX A

To accurately model the atomic dynamics of the ^{87}Rb system subject to a phase-modulated field, we employ the generalized Vanier theory [23] of the 0-0 hyperfine transition in alkali-metal atoms. Briefly, the ground state of an alkali atom has $g = 2(2I + 1)$ Zeeman sublevels (where I is the nuclear spin). Consequently, modeling of the dynamics in the most general form requires the solution of $4(I + 1)$ simultaneous differential equations with nonconstant coefficients (including the real and imaginary parts of the 0-0 coherence), or in the case of ^{87}Rb with $I = 3/2$ ten simultaneous equations. The generalized Vanier model simplifies this considerably by assuming the following: (1) all of the $|F = I + \frac{1}{2}, m_F \neq 0\rangle$ states have the same fractional population; (2) all of the $|F = I - \frac{1}{2}, m_F \neq 0\rangle$ states have the same fractional population; and (3) that there is only one coherence in the system, which is between the $|F = I + \frac{1}{2}, m_F = 0\rangle$ and $|F = I - \frac{1}{2}, m_F = 0\rangle$ states. With these assumptions, the dynamics of any alkali 0-0 hyperfine transition can be described by five simultaneous equations, which after normalizing the density matrix ρ, and using Einstein summation convention become

$$\frac{\partial \rho_i}{\partial t} = -\Lambda_{ij}(z,t)\rho_j + \zeta_i(z), \tag{A1}$$

where

$$\rho = \begin{bmatrix} \rho(\tilde{F}, m_F \neq 0) \\ \rho(\tilde{F}, 0) \\ \rho(F, 0) \\ \text{Re}[\rho(\tilde{F}, 0; F, 0)] \\ \text{Im}[\rho(\tilde{F}, 0; F, 0)] \end{bmatrix}, \tag{A2a}$$

$$\Lambda(z, t) = \begin{bmatrix} \frac{2B(z)}{g}\left(\frac{g}{2} - \tilde{F}\right) + \gamma_1 & -\frac{B(z)}{g} & 0 & 0 & 0 \\ -\frac{2\tilde{F}B(z)}{g} & \frac{B(z)(4I+1)}{g} + \gamma_1 & 0 & 0 & \Omega \\ -\frac{2\tilde{F}B(z)}{g} & -\frac{B(z)}{g} & \gamma_1 & 0 & -\Omega \\ 0 & 0 & 0 & \frac{B(z)}{2} + \gamma_2 & \Delta_o + \alpha\omega_m\,\sin(\omega_m t) \\ 0 & -\frac{\Omega}{2} & \frac{\Omega}{2} & -[\Delta_o + \alpha\omega_m\,\sin(\omega_m t)] & \frac{B(z)}{2} + \gamma_2 \end{bmatrix}, \tag{A2b}$$

$$\zeta = \frac{\gamma_1}{g}\begin{bmatrix} 1 \\ 1 \\ 1 \\ 0 \\ 0 \end{bmatrix}. \tag{A2c}$$

In these expressions, $\tilde{F}$ is the total angular-momentum quantum number for the hyperfine manifold that is coupled to the optical-pumping light, and $B(z)$ is the photon absorption rate, which depends on axial position z as a consequence of attenuation of the light as it passes through the vapor. Assuming that only the first-order axial diffusion mode is effective, we take $B(z) = B_o e^{-\bar{\xi}(z)N\sigma z}$ with the ansatz that

$$\bar{\xi}(z) \cong \frac{2\tilde{F}+1}{2(2I+1)}$$
$$+ \left\{[2\tilde{F}\bar{\rho}_1(z) + \bar{\rho}_2(z)] - \frac{2\tilde{F}+1}{2(2I+1)}\right\}\sin\left(\frac{\pi z}{L}\right); \tag{A3a}$$

here, the overbar indicates a time average. This expression for $\bar{\xi}(z)$ allows for the influence of axial diffusion on the efficiency of optical pumping: at $z = 0$ or L we have $\bar{\xi}(z)$ defined by the degeneracy of the optically pumped Zeeman manifold, while at $z = L/2$ we have $\bar{\xi}(z)$ given by the time-averaged solution of the optically pumped density-matrix equations at that axial location (time averaged over the period of the microwave field's modulation). Since we divide the vapor length into N units (typically $N = 90$), the digitized form of Eq. (A3a) for the numerical solution of

the density-matrix equations is given by

$$\bar{\xi}(z_n) \cong \frac{2\tilde{F}+1}{2(2I+1)}$$
$$+ \left\{[2\tilde{F}\bar{\rho}_1(z_{n-1}) + \bar{\rho}_2(z_{n-1})] - \frac{2\tilde{F}+1}{2(2I+1)}\right\}$$
$$\times \sin\left(\frac{\pi z_n}{L}\right), \tag{A3b}$$

where it is to be noted that $\bar{\xi}(z_n)$ is defined by $\bar{\rho}_1$ and $\bar{\rho}_2$ evaluated at z_{n-1}.

The goal of the computation is to determine the first- and second-harmonic responses of the transmitted light intensity. Thus, we consider light transmission passing through a thin slice of vapor, δz, at time t:

$$\delta\text{I}(t, z) \cong -\bar{I}(z)\,\xi(t, z)\,N\sigma\,\delta z. \tag{A4}$$

Integrating over a normalized length (i.e., $x = z/L$) and then quantizing over the N slices of vapor length yields

$$\frac{\Delta\text{I}(t, L)}{I_o} \cong -\frac{N\sigma L\,\delta x}{B_o}\sum_{n=1}^{N}B(z_n)\,\xi(t, z_n). \tag{A5}$$

The first- and second-harmonic signals, S_1 and S_2 respectively, then become

$$S_1 = \frac{2}{T_o} \int\limits_{t=T_{\text{equil}}}^{T_{\text{equil}}+T_{\text{int}}} \left[\left(\frac{\Delta I(t,L)}{I_o} \right) \right] \sin(\omega_m t) dt$$

$$+ \frac{2}{T_o} \int\limits_{t=T_{\text{equil}}}^{T_{\text{equil}}+T_{\text{int}}} \left[\frac{\Delta I(t,L)}{I_o} \right] \cos(\omega_m t) dt, \qquad \text{(A6a)}$$

$$S_2 = \frac{2}{T_o} \int\limits_{t=T_{\text{equil}}}^{T_{\text{equil}}+T_{\text{int}}} \left[\frac{\Delta I(t,L)}{I_o} \right] \sin(2\omega_m t) dt$$

$$+ \frac{2}{T_o} \int\limits_{t=T_{\text{equil}}}^{T_{\text{equil}}+T_{\text{int}}} \left[\frac{\Delta I(t,L)}{I_o} \right] \cos(2\omega_m t) dt, \qquad \text{(A6b)}$$

where the first term on the right-hand side in each expression is the in-phase component of the harmonic signal, while the second term is the quadrature component. T_{equil} is the time required for the density-matrix equations to reach equilibrium, with T_{int} the time interval over which the time averages are taken for S_1 and S_2. For the present calculations we take $T_{\text{equil}} = 20/\gamma_1$ and $T_{\text{int}} = 60/\gamma_1$. To determine $\xi(t,z_n)$, the density-matrix equations are solved using the Fehlberg fourth-order Runge-Kutta method with adaptive step size [35].

APPENDIX B

In this appendix, we want to sketch out the influence of diffusional relaxation modes on the first and second harmonics of an atom's response to a sinusoidally, phase-modulated field. Given the observable $\langle \vec{I} \cdot \vec{S} \rangle$, which corresponds to the ground-state hyperfine population imbalance in alkali atoms, we write its dynamics as [36]

$$\frac{\partial \langle \vec{I} \cdot \vec{S} \rangle}{\partial t} = D\nabla^2 \langle \vec{I} \cdot \vec{S} \rangle - \gamma_c \langle \vec{I} \cdot \vec{S} \rangle + G(t). \qquad \text{(B1)}$$

Here, $\langle \vec{I} \cdot \vec{S} \rangle = Tr[\rho(\vec{I} \cdot \vec{S})]$, where ρ is the density matrix. The first term on the right-hand side of Eq. (B1) accounts for diffusion of the atoms to the resonance cell walls, with diffusion coefficient D and boundary conditions such that $\langle \vec{I} \cdot \vec{S} \rangle = 0$ at the walls. The second term on the right-hand side corresponds to loss of $\langle \vec{I} \cdot \vec{S} \rangle$ due to binary collisions with the buffer-gas atoms and molecules in the resonance cell, and the third term accounts for first- and second-harmonic forcing functions, which ultimately derive from

the imaginary part of the $\langle \vec{I} \cdot \vec{S} \rangle$ coherence [23]. In particular, as discussed in Appendix A we anticipate that $G \sim \Omega \text{Im}[\rho(\tilde{F}, 0; F, 0)] \equiv \Omega \text{Im}[\rho_{21}]$, where Ω is the Rabi frequency and ρ_{21} is the 0-0 coherence term in the density matrix.

To proceed, we note that in the case $G(t) = 0$, the solution of Eq. (B1) is well known [27]:

$$\langle \vec{I} \cdot \vec{S} \rangle = \sum_{i,\nu} A_{i\nu} J_o(\mu_i \chi) \sin[\pi \nu \zeta] e^{-\gamma_{i\nu} t}, \qquad \text{(B2a)}$$

where

$$\gamma_{i\nu} = \left[\frac{\pi^2 \nu^2}{L^2} + \frac{\mu_i^2}{R_c^2} \right] D + \gamma_c. \qquad \text{(B2b)}$$

In Eqs. (B2), L is the cell length and R_c the cell radius; μ_i is the ith zero of the $J_o(x)$ Bessel function, and ν is an integer: $\chi = r/R$ and $\zeta = z/L$. Further, since Minguzzi *et al.* [28] analyzed an experimental situation very similar to ours (i.e., an optical-pumping light beam with smaller diameter than that of the cylindrical resonance cell), we take from them

$$A_{i\nu} = 4B_o \xi \frac{J_1(\xi \mu_i)}{J_1^2(\mu_i)} \frac{\pi \nu}{\gamma_{i\nu} \mu_i} \left[\frac{1 - (-)^\nu e^{-[\text{Rb}]\sigma L}}{([\text{Rb}]\sigma L)^2 + \pi^2 \nu^2} \right]. \qquad \text{(B3)}$$

Here, $\xi = R_L/R_c$, where $2R_L$ is the diameter of the laser beam, and B_o is a measure of the photon absorption rate at the entrance to the resonance cell.

In what follows, we limit our discussion to $\nu = 1$, as this will simplify the analysis without affecting the implications of our conclusions. Consequently, for the case $G(t) \neq 0$ we write

$$[D\nabla^2 - \gamma_c] \langle \vec{I} \cdot \vec{S} \rangle = -\sum_i \gamma_i f_i(t) J_o(\mu_i \chi) \sin[\pi \zeta], \qquad \text{(B4)}$$

which effectively generalizes Eq. (B2a) to the present situation with the inclusion of $f_i(t)$ on the right-hand side in place of $A_i e^{-\gamma_i t}$. Moreover, since $G(t)$ derives from the $\langle \vec{I} \cdot \vec{S} \rangle$ coherence, it should have a spatial form similar to Eq. (B2a):

$$G(t) = \frac{1}{2} \sum_i G_{o,i} A_i J_o(\mu_i \chi) \sin[\pi \zeta](e^{i\omega_m t} + e^{i2\omega_m t}) + \text{c.c.}; \qquad \text{(B5)}$$

and since $G_{o,i} \sim \Omega \text{Im}[\langle \rho_{21} \rangle]$, we approximate its value by employing a two-level model of the field-atom
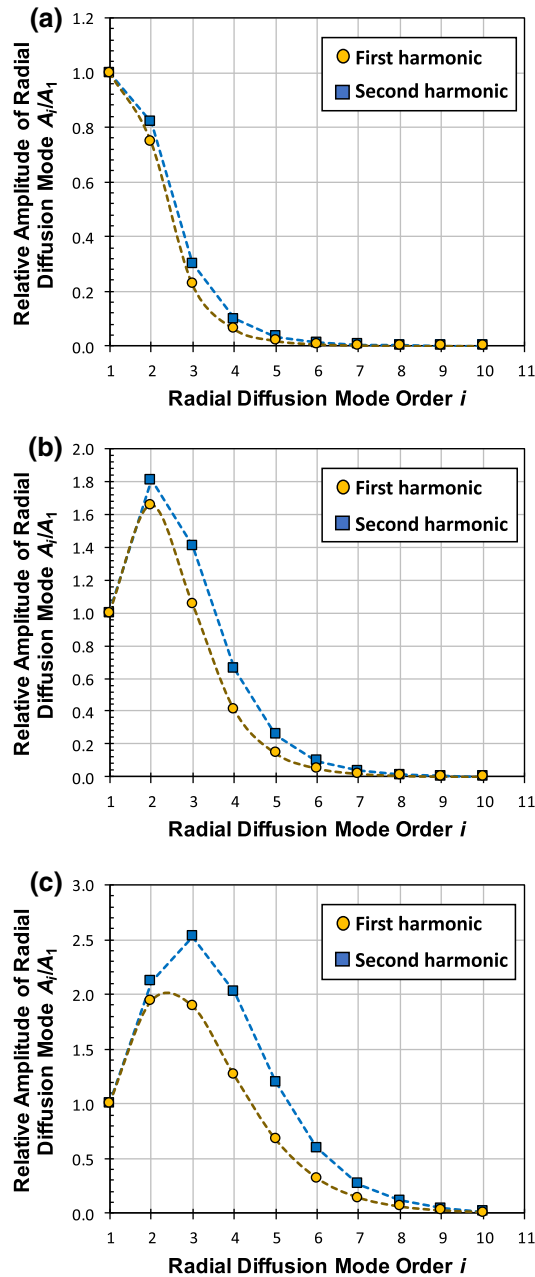
FIG. 8.   The relative amplitude of the ith diffusion mode's contribution to the first- and second-harmonic signals for differing values of the Rabi frequency: $a \Rightarrow \Omega = 30$ Hz, $b \Rightarrow \Omega = 100$ Hz, $c \Rightarrow \Omega = 300$ Hz. At low Rabi frequencies each diffusion mode makes roughly the same contribution to the atom's first and second-harmonic dynamics. However, at larger Rabi frequencies, higher-order diffusion modes play a greater role in the atom's second-harmonic dynamics than they do in the atom's first-harmonic dynamics.

interaction [15]:

$$G_{o,i} = \Omega \, \mathrm{Im}\left[\langle \rho_{21} \rangle \right] \cong \frac{1}{2} \frac{\Omega^2 \gamma_i}{\gamma_i^2 + \Omega^2}. \qquad (B6)$$

Incorporating Eqs. (B4)–(B6) into Eq. (B1), we get

$$\sum_i (\dot{f}_i + \gamma_i f_i) J_o(\mu_i \chi) = \frac{1}{4} \sum_i \left(\frac{\Omega^2 \gamma_i}{\Omega^2 + \gamma_i^2} \right)$$
$$\times A_i J_o(\mu_i \chi)(e^{i\omega_m t} + e^{i2\omega_m t}) + \text{c.c.}, \qquad (B7)$$

which, after taking advantage of the orthonormality of Bessel functions, yields

$$\dot{f}_i + \gamma_i f_i = \frac{1}{4} \left(\frac{\Omega^2 \gamma_i A_i}{\Omega^2 + \gamma_i^2} \right) (e^{i\omega_m t} + e^{i2\omega_m t}) + \text{c.c.} \qquad (B8)$$

Defining the Fourier transform of $f_i(t)$ as $F_i(\omega)$: $f_i(t) = (2\pi)^{-1} \int F_i(\omega) e^{i\omega t} d\omega$, and taking the Fourier transform of Eq. (B8), we get

$$F_i(\omega) = \frac{\pi}{2} \left(\frac{\Omega^2 \gamma_i A_i}{\Omega^2 + \gamma_i^2} \right) \left(\frac{\gamma_i - i\omega}{\gamma_i^2 + \omega^2} \right) [\delta(\omega - \omega_m)$$
$$+ \delta(\omega + \omega_m) + \delta(\omega - 2\omega_m) + \delta(\omega + 2\omega_m)]. \qquad (B9)$$

Finally, taking the inverse Fourier transform we obtain for $f_i(t)$ [with $\varphi_{k,i} = \tan^{-1}(\gamma_i / k\omega_m)$]

$$f_i(t) = \frac{1}{2} \left(\frac{\Omega^2 \gamma_i A_i}{\Omega^2 + \gamma_i^2} \right)$$
$$\times \left[\frac{\sin(\omega_m t + \varphi_{1,i})}{\sqrt{\gamma_i^2 + \omega_m^2}} + \frac{\sin(2\omega_m t + \varphi_{2,i})}{\sqrt{\gamma_i^2 + 4\omega_m^2}} \right]. \qquad (B10)$$

Figure 8 shows the various diffusion modes' contributions to the first and second-harmonic signals for three different values of the Rabi frequency. For the computation, we use parameter values from our experiment, approximating $\gamma_c = 10$ Hz. (Note that our experimentally measured dephasing rate is a combination of γ_c *plus* diffusion.) Clearly, at Rabi frequencies corresponding to the optimum in our experiments (i.e., $\Omega \sim \omega_m$) and larger, higher-order diffusion modes play a more significant role in the atom's second-harmonic dynamics than they do in the atom's first-harmonic dynamics. This is what we hypothesize to explain the experimental results shown in Figs. 6 and 7.

[1] J. Vanier, M. Têtu, and L.-G. Bernier, Transfer of frequency stability from an atomic reference to a quartz-crystal oscillator, IEEE Trans. Instrum. Meas. **28**, 188 (1979).

[2] J. Camparo and G. Fathi, The 2nd-harmonic signal in vapor-cell clocks & error-signal quality: Does S₂ imply dS₁/dΔ, in *Proc. 2013 IEEE UFFC, EFTF and PFM Symposium* (IEEE Press, Piscataway, NJ, 2013), pp. 224–227.

[3] B. Jaduszliwer and J. P. Hurrell, Second harmonic level monitors in cesium atomic frequency standards, in *Proc. 1994 IEEE Internat. Freq. Control Symp.* (IEEE Press, Piscataway, NJ, 1994), pp. 759–775.

[4] B. Ghosal and G. M. Saxena, Design verification model of rubidium frequency standard for space, J. Mod. Phys. **5,** 128 (2014).

[5] J. Vanier and L.-G. Bernier, On the signal-to-noise ratio and short-term stability of passive rubidium frequency standards, IEEE Trans. Instrum. Meas. **30,** 277 (1981).

[6] J. C. Camparo and R. P. Frueholz, A dressed atom interpretation of adiabatic rapid passage, J. Phys. B: At. Mol. Phys. **17,** 4169 (1984).

[7] R. P. Frueholz and J. C. Camparo, Microwave field strength measurement in a rubidium clock cavity via adiabatic rapid passage, J. Appl. Phys. **57,** 704 (1985).

[8] D. Bohm, *Quantum Theory* (Prentice-Hall, Englewood Cliffs, New Jersey, 1951).

[9] L. I. Schiff, *Quantum Mechanics* (McGraw-Hill, New York, NY, 1955).

[10] J. Speidel, M. Tossaint, S. Wallner, J. A. Ávila-Rodríguez, Integrity for aviation: Comparing future concepts, Inside GNSS, July/August 2013, pp. 54–64.

[11] Y. C. Chan, W. A. Johnson, S. K. Karuza, A. M. Young, and J. C. Camparo, Self-monitoring and self-assessing atomic clocks, IEEE Trans. Instrum. Meas. **59,** 330 (2010).

[12] J. C. Camparo, Atomic Stabilization of Electromagnetic Field Strength Using Rabi Resonances, Phys. Rev. Lett. **80,** 222 (1998).

[13] M. Kinoshita and M. Ishii, Electromagnetic field sensor based on atomic candle, IEEE Trans. Instrum. Meas. **66,** 1592 (2017).

[14] X. Liu, Z. Jiang, J. Qu, D. Hou, X. Huang, and F. Sun, Microwave magnetic field detection based on Cs vapor cell in free space, Rev. Sci. Instrum. **89,** 063104 (2018).

[15] J. G. Coffer, B. Sickmiller, A. Presser, and J. C. Camparo, Line shapes of atomic-candle-type Rabi resonances, Phys. Rev. A **66,** 023806 (2002).

[16] A. Tretiakov and L. J. LeBlanc, Microwave Rabi resonances beyond the small-signal regime, Phys. Rev. **99,** 043402 (2019).

[17] D. Kuksenkov, S. Feld, C. Wilmsen, H. Temkin, S. Swirhun, and R. Leibenguth, Linewidth and α-factor in AlGaAs/GaAs vertical cavity surface emitting lasers, Appl. Phys. Lett. **66,** 277 (1995).

[18] W. Happer, Optical pumping, Rev. Mod. Phys. **44,** 169 (1972).

[19] L. C. Balling, in *Advances in Quantum Electronics*, edited by D. W. Goodwin (Academic Press, New York, 1975), Vol. 3, pp.1–166.

[20] J. C. Camparo, Saturation broadening by inhomogeneous fields, Phys. Rev. A **39,** 69 (1989).

[21] A. Hudson and J. Camparo, Mesoscopic physics in vapor-phase atomic systems: Collision-shift gradients and the 0-0 hyperfine transition, Phys. Rev. **98,** 042510 (2018).

[22] In the time between the studies of Ref. [21] and the present studies, we discovered that β had changed slightly, which is likely due to slight changes in the VSWR of the 6.8-GHz signal path and/or changes in the orientation of the microwave horn. We are able to account for this change by comparing the microwave power needed for saturation of the 0-0 resonance in the previous studies to the microwave power needed for saturation in the present studies.

[23] J. C. Camparo and R. P. Frueholz, Linewidths of the 0-0 hyperfine transition in optically pumped alkali-metal vapors, Phys. Rev. A **31,** 1440 (1985).

[24] M. Huang, J. G. Coffer, and J. C. Camparo, ^{87}Rb hyperfine-transition dephasing in mixed buffer-gas systems, Phys. Rev. A **75,** 052717 (2007).

[25] E. Bernabeu and J. Tornos, Influence of optical factors on the relaxation signal of an optically pumped vapor, J. Opt. Soc. Am. B **1,** 586 (1984).

[26] J. C. Camparo, The influence of diffusional relaxation on the clock signal in the laser-pumped rubidium atomic frequency standard, Aerospace Report No. TOR-2017-00316, 5 December 2016.

[27] F. A. Franz, Relaxation at cell walls in optical-pumping experiments, Phys. Rev. A **6,** 1921 (1972).

[28] P. Minguzzi, F. Strumia, and P. Violino, Temperature effects in the relaxation of optically oriented alkali vapours, Il Nuovo Cimento **46B,** 145 (1966).

[29] V. Formichella, J. Camparo, I. Sesia, G. Signorile, L. Galleani, M. Huang, and P. Tavella, The ac stark shift and space-borne rubidium atomic clocks, J. Appl. Phys. **120,** 194501 (2016).

[30] V. Formichella, J. Camparo, and P. Tavella, Influence of the ac-Stark shift on GPS atomic clock timekeeping, Appl. Phys. Lett. **110,** 043506 (2017).

[31] J. C. Camparo and R. P. Frueholz, A three-dimensional model of the gas cell atomic frequency standard, IEEE Trans. Ultrason., Ferroelec., Freq. Control **36,** 185 (1989).

[32] R. J. Chaffin, Neutron damage effects in step recovery diode frequency multipliers, IEEE Trans. Nuclear Sci. **18,** 366 (1971).

[33] J. G. Coffer, B. Sickmiller, and J. Camparo, Cavity-Q aging observed via an atomic candle signal, IEEE Trans. Ultrason., Ferroelec., Freq. Control **51,** 139 (2004).

[34] J. Kitching, S. Knappe, and E. A. Donley, Atomic sensors – A review, IEEE Sens. J. **11,** 1749 (2011).

[35] W. Cheney and D. Kincaid, *Numerical Mathematics and Computing* (Brooks/Cole Publishing Co., Monterey, CA, 1985), Chs. 8 & 11.

[36] N. Beverini, P. Minguzzi, and F. Strumia, Foreign-gas-induced cesium hyperfine relaxation, Phys. Rev. A **4,** 550 (1971).